Journal of Superconductivity and Novel Magnetism (2020) 33:3051–3058
https://doi.org/10.1007/s10948-020-05533-y

ORIGINAL PAPER

Ni-Doped SnO_2 Dilute Magnetic Semiconductors: Morphological Characteristics and Optical and Magnetic Properties

Feng Jiang [1] · **Lizhi Peng** [1] · **Tianfu Liu** [1]

Received: 2 February 2020 / Accepted: 30 April 2020 / Published online: 5 June 2020

Abstract

Ni-doped SnO_2 dilute magnetic semiconductors were prepared by precipitation method. The obtained spherical nanoparticles are pure tetragonal rutile phase, and Ni ions promote the growth of SnO_2 nanoparticles. The optical band gap energy of the SnO_2 nanoparticles decreases from 3.14 to 2.84 eV when input $x\%$ Ni. The room-temperature photoluminescence (PL) spectra and X-ray photoelectron spectroscopy (XPS) confirm the existence of surface oxygen vacancies caused by the large specific surface area and the introduction of Ni ions. All the synthesized Ni-doped SnO_2 nanoparticles achieve room-temperature ferromagnetism, with a saturation magnetization of up to 2.95×10^{-3} emu/g at a dopant concentration of 2%. The interaction between oxygen vacancies and Ni^{2+} realizes the magnetic transition of nanoparticles from diamagnetic to ferromagnetic.

Keywords SnO_2 nanoparticle · Morphology · Optical property · Magnetic property

1 Introduction

Traditional electronic devices take advantage of the conductivity of electrons, ignoring the spin characteristics that are closely related to information manipulation and storage [1]. Spintronics is a science that studies the charge transport and spin of electrons. Finding material for new generation spintronic devices is an ongoing quest. Diluted magnetic semiconductor (DMS) with a Curie temperature (*Tc*) well above room temperature (RT) is considered a promising candidate. The main challenge for DMS is to achieve RT spin injection. Early DMSs have a *Tc* below RT, which limited its application in spintronic devices [2].

Matsumoto et al. observed long-range ferromagnetic coupling in Co-doped TiO_2 films for the first time, paving the way for oxide-based DMSs [3]. Doping transition metal in oxides has achieved RT ferromagnetism, such as ZnO, In_2O_3, CeO_2, and SnO_2 [4–7]. Among these oxides, SnO_2 is a natural non-stoichiometric oxide with intrinsic defects (oxygen vacancies and interstitial tin). SnO_2, as a typical wide band gap (3.6 eV [8]) n-type semiconductor has widespread applications in solar cells [9], gas sensors [10, 11], photocatalysts [12], etc. Besides, its excellent optical transmittance and low resistivity are attractive for DMSs.

Usually, pure SnO_2 is diamagnetic for the $4d^{10}$ electronic configuration of Sn. A density functional study showed that even pure SnO_2 is magnetic due to the presence of Sn vacancy, which shows the importance of defects to ferromagnetic coupling [13]. The defects in the SnO_2 are sensitive to the preparation method and environment. Mehraj et al. studied the effect of annealing temperature on magnetic properties [14]. The study showed that oxygen vacancies decrease with increasing annealing temperature, leading to a decrease in saturation magnetization. Similarly, Zhang et al. prepared SnO_2 at different oxygen flow rates and demonstrated the importance of oxygen vacancies for magnetism [15]. In addition to controlling experimental conditions, doping transition metal provides an efficient strategy to break crystal lattice symmetry. The radius difference between dopant ions and host ions, the charge mismatch, etc. inevitably increases the concentration of defects in the sample. The interaction between dopant ions and defects is also highly debatable. Transition metals (such as Fe, Co, Ni, Mn, and Cr) are usually used to tailor the magnetic property of semiconductors. Ni ions are commonly used as dopant in SnO_2-based DMSs. In 2005, Archer et al. reported Ni-doped SnO_2 DMS system [8]. After that, with the improvement of the preparation method, Ni-doped SnO_2 with various morphologies such as nanorods [16] and nanofilms [17] also

---

✉ Tianfu Liu
liutf@bit.edu.cn

[1] School of Chemistry and Chemical Engineering, Beijing Institute of Technology, Beijing 102488, People's Republic of China

achieved the RT ferromagnetism. These interesting findings are of great significance for the study of SnO_2-based DMSs.

In this report, we prepared uniform Ni-doped SnO_2 DMSs through precipitation method. In order to understand the mechanism of ferromagnetic interaction in Ni-doped SnO_2 nanoparticles, the morphology and optical properties of the sample were explored. It is observed that Ni ions and oxygen vacancies play a vital role in ferromagnetic coupling. Therefore, transition metal ions and oxygen vacancies are essential in oxide-based DMSs.

2 Synthesis of Pure and Ni-Doped SnO_2 Nanoparticles

All used reagents were not further purified. 0–3% (mole fraction) Ni-doped SnO_2 nanoparticles were prepared by precipitation method. In a typical procedure, 1 g stannic chloride ($SnCl_4{\cdot}5H_2O$, purity 99%) was dissolved in distilled water under continuous stirring. Aqueous ammonia (1 M) was added dropwise to the above solution until pH value reached ~ 9 and kept stirring for 1 h to ensure the complete reaction. The white precipitate was collected by centrifugation and washed with distilled water and ethanol several times to remove impurities (precipitate A). Appropriate stoichiometric ratio nickel chloride ($NiCl_2{\cdot}6H_2O$, purity 98%) was dissolved in distilled water under stirred. 1 M NaOH was subsequently dropped into the above solution until pH reached 10 to ensure complete Ni^{2+} precipitation. The obtained green precipitate was collected and washed with distilled water (precipitate B). Precipitation A and B were poured into 10 ml ethanol and continuously stirred for 12 h to obtain a homogeneous mixture. The obtained gels were collected and dried at 80 °C for 12 h. All samples finally were calcined at 400 °C for 4 h in air.

3 Characterization

Crystalline structure and impurity phase were confirmed by powder X-ray diffraction (PXRD) (Bruker, D-8 Advance, Cu K_α radiation, $\lambda = 1.5406$ Å) with scanning rate 2° and angle range 20–80°. The microscopic morphologies of the nanoparticles were observed with a field emission scanning electron microscope (FE-SEM, JSM-7500F). High-resolution transmission electron microscopy was used to observe the microstructure of nanoparticles (HRTEM, JEM-2100F). Room-temperature magnetic property was manifested by a superconducting quantum interference device (SQUID, MPMS-XL-7). UV–Vis absorption spectra were recorded using a solid double beam UV–visible spectrometer (TU-1901) in the wavelength range 200–600 nm. The surface defects of the material can be identified by photoluminescence (PL, F-7000) spectra. X-ray photoelectron spectroscopy (XPS) spectrum recorded on the Thermo Fisher Scientific Multilab 250xi instrument with Al K_α radiation (1486.6 eV).

4 Results and Discussion

4.1 Structure and Morphologies

The XRD patterns of 0–3% Ni-doped SnO_2 are shown in Fig. 1. All diffraction peaks can be indexed as a tetragonal rutile structure of SnO_2 with space group $P4_2/mnm$ (JCPDS file no. 41-1445). There are no peaks of the impurity phase within the detection limit, which indicates that Ni atoms are incorporated into SnO_2 lattice instead of forming into a secondary phase (NiO or Ni_2O_3). After doping with nickel, the XRD diffraction peaks of the samples did not shift to low or high angles. This is because the Ni^{2+} and Sn^{4+} have the same ion radius, both being 0.69 Å. The values of lattice parameters calculated by XRD patterns are displayed in Table 1. The lattice parameters do not change much, indicating that Ni^{2+} ions have successfully replaced Sn^{4+} sites in the lattice. The XRD diffraction peak and variation of lattice parameters confirm that Ni successfully doped into SnO_2 lattice rather than to form secondary phase or Ni clusters.

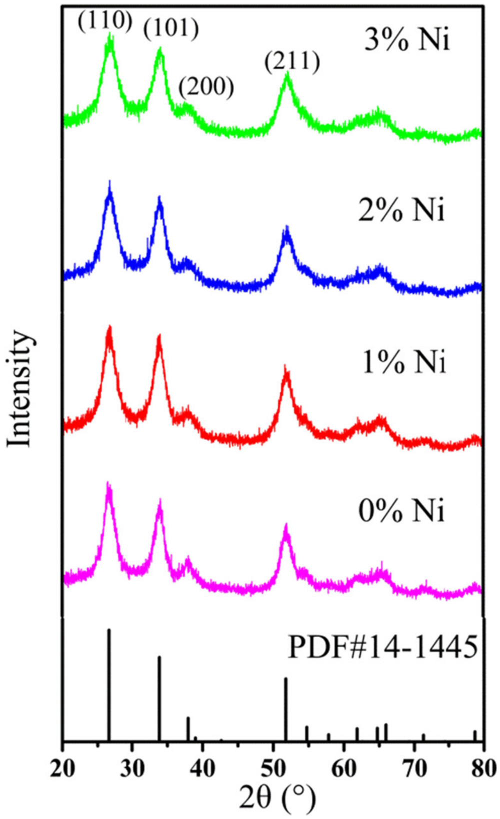

Fig. 1 XRD patterns of 0–3% Ni-doped SnO_2

Table 1 Lattice constants of 0–3% Ni-doped SnO_2

Ni content	0%	1%	2%	3%
a (Å)	4.7274	4.7243	4.7206	4.7197
c (Å)	3.1743	3.1676	3.1714	3.1657

Figure 2 depicts the pure and Ni-doped SnO_2 SEM micrographs. It is observed that all samples are nearly spherical in shape and agglomerated to decrease surface energy. It can be seen from SEM images that Ni does not cause remarkable morphological changes of nanoparticles. TEM was used to further explore the morphology and particle size. It can be seen from the TEM images that the particle size first increases and then decreases. When the Ni concentration is 1%, the value of nanoparticle size reaches the largest, about 10–20 nm. Generally, the doping of Ni limited the SnO_2 grain growth, resulting in a decrease in the crystallinity of the sample and particle size. In the present case, the lower calcination temperature and less calcination time caused the crystallinity of the sample to decrease, making it unable to grow following the normal [001] direction (*c*-axis) [18]. The introduction of a small amount of Ni (1%) promoted this growth mode of the sample and the particle size larger. A study has shown that in Ni-doped SnO_2 system, surface segregation can occur at concentrations greater than 2% [19]. When the doped concentration increases, the particles become smaller due to the limited solubility of the solid solution and surface segregation. The microstructure of nanoparticles was further studied by HRTEM (Fig. 3). The lattice spacing can be estimated through HRTEM images. For pure SnO_2, the planar spacing of 0.332 nm and 0.278 nm can be indexed to lattice spacing of (110) and (101) of rutile SnO_2, respectively. For 3% Ni-doped SnO_2, these two lattice spacings are 0.333 nm and 0.281 nm.

4.2 Optical Properties

UV–vis spectroscopy is a powerful means to characterize optical absorbance properties and optical band gaps of materials. Figure 4 shows the RT optical absorption spectra of different contents of Ni-doped SnO_2. The absorbance of materials is affected by grain size, surface defects, and optical band gap. All samples show a broad absorption band at visible region due to the photoexcitation of electrons from valence band to the conduction band [20]. The UV–visible absorption edge shifts to the longer wavelength region after doping Ni. The introduction of Ni causes the electron wave function to overlap, leading to the narrower band gap and red shift of UV–visible absorption edge.

The optical band gap can be estimated by Tauc's plot:

$$ahv = A\left(hv - E_g\right)^n \tag{1}$$

where α is the absorption coefficient, A is a constant for a direct transition, h is the Planck's constant, ν is the frequency of the incident photon, and E_g is the optical band gap. The value of 'n' depends on the type of transition. For the direct band gap semiconductor, this value is 1 / 2 [21]. In the present case, $\alpha = 2.303 \times$ Absorbance / t; t is the thickness of the material. Figure 5 shows the Tauc's plot $(\alpha h\nu)^2$ versus $h\nu$. E_g is the intersection with the *x*-axis after extending the linear part of the curve. For 0%, 1%, 2%, and 3% Ni-doped SnO_2 samples, the band gaps are 3.14 eV, 2.90 eV, 2.88 eV, and 2.87 eV, respectively. It is noted that all samples have an energy band

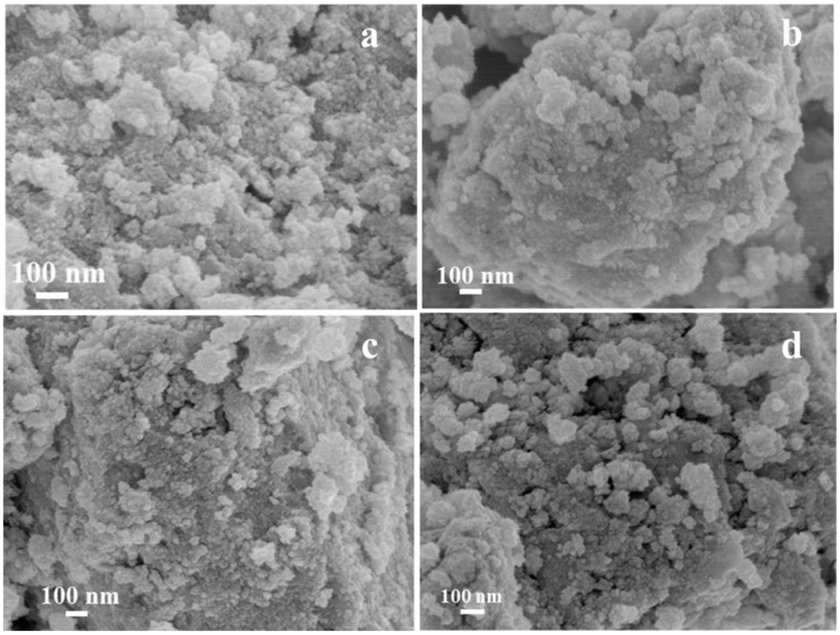

Fig. 2 SEM micrographs of different Ni-doped SnO_2 contents. **a** 0%; **b** 1%; **c** 2%; **d** 3%

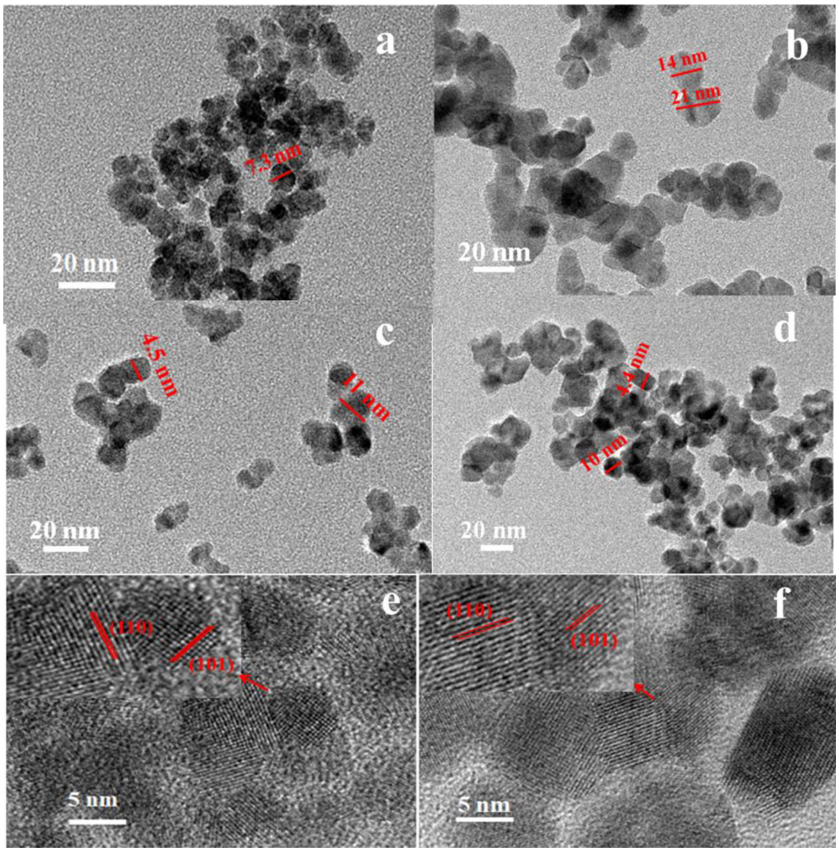

Fig. 3 TEM micrographs of different Ni-doped SnO_2 contents. **a** 0%; **b** 1%; **c** 2%; **d** 3%. HREM micrographs of 0% (**e**) and 3% (**f**) Ni-doped SnO_2

gap smaller than that of the bulk one ($E_g = 3.6$ eV). Defects generated during the calcination process introduce a new impurity band between the conduction band and the forbidden band, resulting in a narrower optical band gap. Compared with pure SnO_2, the E_g of Ni-doped SnO_2 is further decreased to about 0.2 ~ 0.3 eV. This decrease in band gap indicates the substitution of Sn sites by Ni ions in SnO_2. This phenomenon is common in transition metal-doped systems, which can be attributed to the sp-*d* exchange interactions between band electrons and the localized *d* electrons of the transition metal ions [22–24].

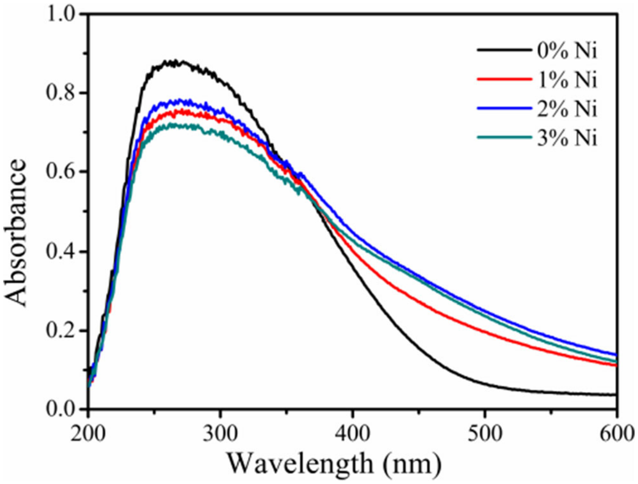

Fig. 4 UV–vis absorption spectra for 0–3% Ni-doped SnO_2

Bulk SnO_2 has no PL property, while it occurs when the particle size reaches the nanometer level [25]. Transition metal doping can cause changes in the exciton structure of the sample, which can be characterized by RT PL spectroscopy. All excitation spectra of samples were recorded at an emission wavelength of 370 nm and are shown in Fig. 6. For metal oxides, oxygen vacancies are the main component of defects and serve as radiative centers in the process of luminescence. There are three types of oxygen vacancies in the host and doped materials, neutral oxygen vacancy (V_O), singly charged oxygen vacancy (V_O^+), and doubly charged oxygen vacancy (V_O^{++}), respectively. For all samples, emission peaks were observed at around 420 nm and 470 nm. Blue emission band at about 420 nm can be generated due to the recombination of a conduction band electron with a V_O^{++} center [26, 27]. After photoexcitation, electrons are excited from the valence band to the conduction and left holes in the valence band. These active holes can be trapped at the V_O^+ to form V_O^{++}. The blue excitation wave occurs when a trapped hole is combined with a conduction band electron [28]. The peak at 470 nm is due to defect levels in the band gap [29].

Figure 7 displays the core-level spectra of O 1s, Sn 3d, and Ni 2p peaks of 0% and 3% Ni-doped SnO_2 samples. The valence state of Ni in the sample was analyzed through the

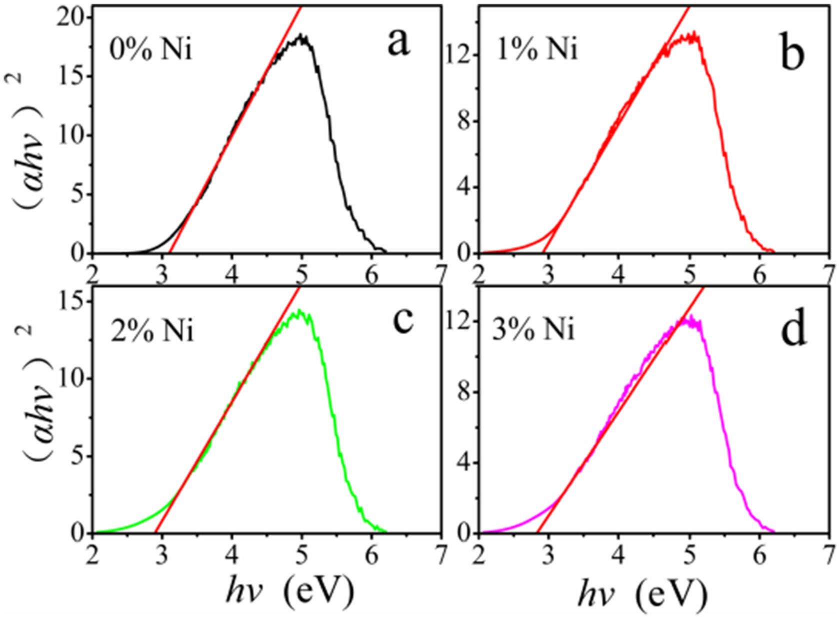

Fig. 5 $(\alpha h\nu)^2$ versus $h\nu$ plots for 0–3% Ni-doped SnO_2

XPS curves. The peaks centered at 495.50 eV and 487.10 eV with a spin energy separation of 8.4 eV corresponding to $3d_{3/2}$ and $3d_{5/2}$ levels of Sn^{4+}, respectively [30, 31]. The absence of shoulder peaks in the XPS spectrum demonstrates that the Sn in the sample is only in the + 4 valence state. After doping Ni (3%), the coordination environment of Sn^{4+} changes and the binding energy decreases about 0.37 eV. The shift in the binding energies is due to the interfacial electron transfer due to the interaction between interface Ni and SnO_2 [32]. The asymmetric O 1s spectrum can be Gaussian fitted into two peaks. The lower binding energy peak arises due to O-Sn-O bond [33], while the higher binding energy peaks may be attributed to chemisorbed oxygen (-OH) [22]. And the component of higher binding energy peak increases from 0.216 to 0.352 as the Ni content up to 3%. When the sample is doped with Ni, the oxygen vacancies increase due to the charge imbalance of Sn^{4+} and Ni^{2+}. Hence, a large number of free oxygen molecules can be chemisorbed on the surface of nanoparticles [34]. The binding energy curve of Ni 2p (3% Ni-doped SnO_2) is shown in Fig. 7. The Gaussian peak centered at 855.97 eV corresponds to Ni $2p_{3/2}$ of + 2 state [35].

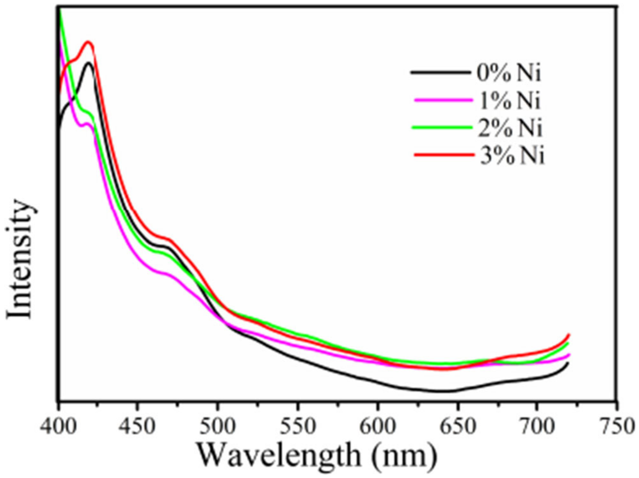

Fig. 6 PL spectra of 0–3% Ni-doped SnO_2

4.3 Magnetic Property

Magnetization versus magnetic field (*M–H*) curves of SnO_2 with different Ni concentrations is shown in Fig. 8. The inset is the *M–H* curve of pure SnO_2. All Ni-doped SnO_2 nanoparticles clearly exhibit hysteresis behavior, confirming the ferromagnetism of the samples. Generally, since there are no unpaired electrons for $4d^{10}$ electronic structure of Sn^{4+}, pure SnO_2 is diamagnetic [36, 37].

The values of saturation magnetization (M_s), coercive field (H_c), and remnant magnetizations (M_r) are mentioned in Table 2. When the doping Ni concentration is increased from 1 to 2%, the value of M_s is increased from 1.49×10^{-3} to 2.95×10^{-3} emu/g. When the Ni doping concentration is 3%, the total magnetization of the sample is the sum of the ferromagnetic portion and the paramagnetic portion, and the saturation magnetization is also reduced to 1.84×10^{-3} emu/g. The phenomenon of paramagnetic signals appearing with the increase of the doping concentration of transition metals also appears in other metal oxide doping systems [38, 39].

The physical and chemical properties of materials are often inseparable from the morphology. Different morphologies of SnO_2 formed during the calcination process have various types and number of defects, which in turn leads to changes in the magnetic properties of the sample. In Ni-doped SnO_2

Fig. 7 Comparison of O 1s and Sn 3d core-level spectra of 0% and 3% Ni-doped SnO_2 nanoparticles. Ni $2p_{3/2}$ core-level spectrum of 3% Ni-doped SnO_2 nanoparticles

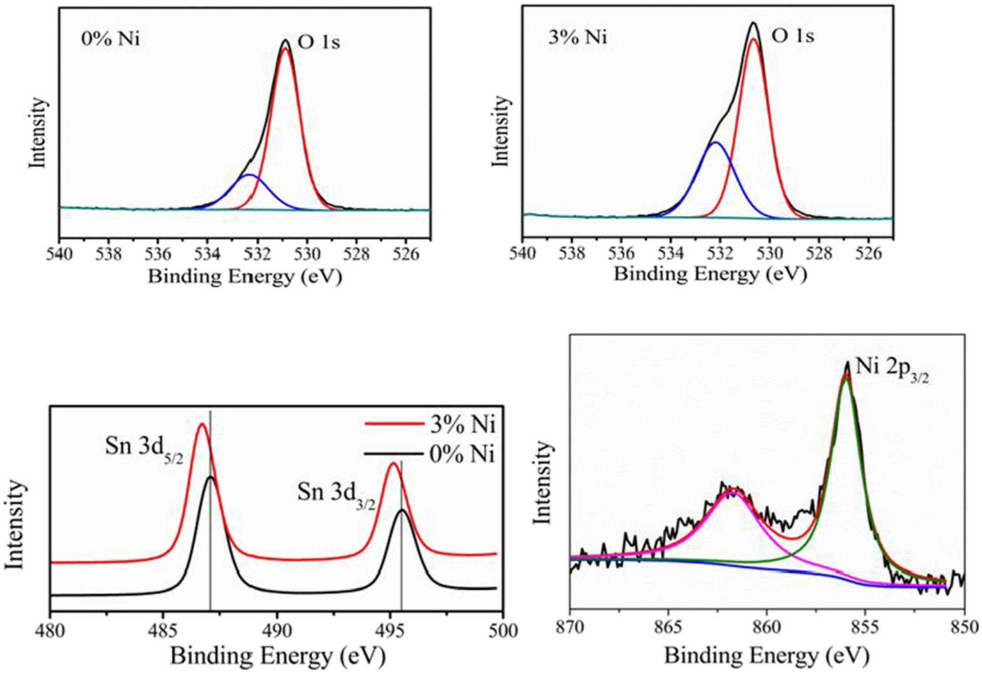

with different morphologies, the spherical nanoparticles are ferromagnetic [23, 36, 40], while the popcorn-like samples are diamagnetic [21]. In this work, the Ni-doped SnO_2 nearly spherical nanoparticles are ferromagnetic. Combining previous reports with our work, it is concluded that there is an internal relationship between the magnetism and morphology of the sample. It seems that for Ni-doped SnO_2, the spherical nanoparticles are easier to become ferromagnetic. Although morphology has an influence on magnetism, it is not conclusive, and the ferromagnetic coupling effect must be analyzed in detail. Coey et al. proposed two important theories of ferromagnetic coupling of DMS-bound magnetic polarons (BMPs) [41] and F-Center Exchange [42]. In our experiment, there are a large number of oxygen vacancies in pure and Ni-doped samples observed by PL spectra and XPS, but ferromagnetic coupling occurs only in the doped samples, which proves that ferromagnetism is closely related to Ni^{2+}. Wang et al. used the first principle to calculate the ferromagnetic origin of Ni-doped SnO_2 and found that oxygen vacancies play an important role in long-range ferromagnetic coupling [43]. The doping concentration of Ni is well below the percolation limit (≈ 0.25). So the ferromagnetic order in 1% and 2% Ni-doped SnO_2 cannot be attributed to the super-exchange or double-exchange interaction of Ni clusters [44]. In summary, we speculate that the magnetism in the sample is related to the interaction between Ni^{2+} and oxygen vacancies. The specific mode of action can be explained by the BMP theory. The electrons trapped in oxygen vacancies can interact with the localized spins of Ni^{2+} ions, forming a bound magnetic polaron (BMP). A great number of BMPs overlap to realize long-range ferromagnetic order [23, 45]. However, when the Ni concentration is increased to 3%, the paramagnetic signal appears in the sample. As the Ni doping concentration increases, the probability of Ni^{2+}-O^{2-}-Ni^{2+} increases, and a well-known super-exchange interaction occurs (antiferromagnetic coupling), leading to the observed decrease in magnetic moment.

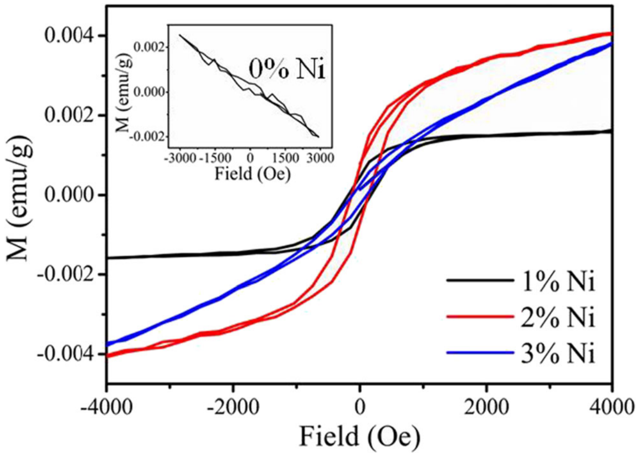

Fig. 8 *M–H* curves of Ni dope SnO_2 at RT. Insert is the *M–H* curve of pure SnO_2

Table 2 Magnetic parameters obtained from the fit of M versus H curves

Ni content	$M_r \times 10^{-4}$ (emu/g)	H_c (Oe)	$M_s \times 10^{-3}$ (emu/g)
1%	4.588	170.71	1.49
2%	7.626	125.76	2.95
3%	2.752	116.06	1.86

5 Conclusion

Precipitation method can be used to prepare uniform Ni-doped SnO_2 dilute magnetic semiconductors. XRD and UV–Vis spectra indicate that Ni ions have successfully replaced the Sn sites in the lattice. PL spectra and XPS confirm the existence of oxygen vacancies in the sample. The interaction between Ni^{2+} and oxygen vacancies causes ferromagnetic coupling, which can be explained by the BMP theory. The SnO_2-based DMS prepared by this method has an optimal Ni doping concentration of 2%.

Funding Information This work was supported by the National Natural Science Foundation of China (21571018).

References

1. Garnet, N.S., Ghodsi, V., Hutfluss, L.N., Yin, P., Hegde, M., Radovanovic, P.V.: Probing the role of dopant oxidation state in the magnetism of diluted magnetic oxides using Fe-doped In_2O_3 and SnO_2 nanocrystals. J. Phys. Chem. C. **121**(3), 1918–1927 (2017)
2. Novak, V., Olejnik, K., Wunderlich, J., Cukr, M., Vyborny, K., Rushforth, A.W., Edmonds, K.W., Campion, R.P., Gallagher, B.L., Sinova, J., Jungwirth, T.: Curie point singularity in the temperature derivative of resistivity in (Ga,Mn)As. Phys. Rev. Lett. **101**(7), 077201 (2008)
3. Matsumoto, Y., Murakami, M., Shono, T., Hasegawa, T., Fukumura, T., Kawasaki, M., Ahmet, P., Chikyow, T., Koshihara, S., Koinuma, H.: Room-temperature ferromagnetism in transparent transition metal-doped titanium dioxide. Science. **291**(5505), 854–856 (2001)
4. Singhal, A., Achary, S.N., Manjanna, J., Chatterjee, S., Ayyub, P., Tyagi, A.K.: Chemical synthesis and structural and magnetic properties of dispersible cobalt- and nickel-doped ZnO nanocrystals. J. Phys. Chem. C. **114**(8), 3422–3430 (2010)
5. Doke, S., Sonawane, K., Banerjee, A., Mahamuni, S.: Evidence of various stabilizing mechanisms in ferromagnetic Co doped ZnO nanocrystals. J. Alloys Compd. **726**, 947–954 (2017)
6. Yang, Z.G., Zhao, Z.J., Yu, J.B., Li, J.Y., Ren, Z.M., Ma, S.Q., Ren, S.X., Yu, G.: Effect of Co substitution and magnetic field on the morphologies and magnetic properties of CeO_2 nanoparticles. Ceram. Int. **45**(9), 11927–11933 (2019)
7. Luo, X., Tseng, L.T., Wang, Y.R., Bao, N.N., Lu, Z.M., Ding, X., Zheng, R.K., Du, Y.H., Huang, K., Shu, L., Suter, A., Lee, W.T., Liu, R., Ding, J., Suzuki, K., Prokscha, T., Morenzoni, E., Yi, J.B.: Intrinsic or Interface clustering-induced ferromagnetism in Fe-doped In_2O_3-diluted magnetic semiconductors. ACS Appl. Mater. Interfaces. **10**(26), 22372–22380 (2018)
8. Archer, P.I., Radovanovic, P.V., Heald, S.M., Gamelin, D.R.: Low-temperature activation and deactivation of high-curie-temperature ferromagnetism in a new diluted magnetic semiconductor: Ni^{2+}-doped SnO_2. J. Am. Chem. Soc. **127**(41), 14479–14487 (2005)
9. Jiang, Q., Zhang, X.W., You, J.B.: SnO_2 : a wonderful electron transport layer for perovskite solar cells. Small. **14**(31), e1801154 (2018)
10. Kuang, Q., Lao, C.S., Wang, Z.L., Xie, Z.X., Zheng, L.S.: High-sensitivity humidity sensor based on a single SnO_2 nanowire. J. Am. Chem. Soc. **129**(19), 6070–6071 (2007)
11. Zhang, S.Y., Yin, C.B., Yang, L., Zhang, Z.L., Han, Z.J.: Investigation of the H_2 sensing properties of multilayer mesoporous pure and Pd-doped SnO_2 thin film. Sensors Actuators B Chem. **283**, 399–406 (2019)
12. Chu, D.Q., Zhu, S.P., Wang, L.M., Wang, G.W., Zhang, N.: Hydrothermal synthesis of hierarchical flower-like Zn-doped SnO_2 architectures with enhanced photocatalytic activity. Mater. Lett. **224**, 92–95 (2018)
13. Rahman, G., García-Suárez, V.M., Hong, S.C.: Vacancy-induced magnetism in SnO_2: a density functional study. Phys. Rev. B. **78**, 184404 (2008)
14. Mehraj, S., Ansari, M.S., Al-Ghamdi, A.A.: Alimuddin: annealing dependent oxygen vacancies in SnO_2 nanoparticles: structural, electrical and their ferromagnetic behavior. Mater. Chem. Phys. **171**, 109–118 (2016)
15. Zhang, L., Ge, S.H., Zuo, Y.L., Zhang, B.M., Xi, L.: Influence of oxygen flow rate on the morphology and magnetism of SnO_2 nanostructures. J. Phys. Chem. C. **114**(17), 7541–7547 (2010)
16. Srinivas, K., Rao, S.M., Reddy, P.V.: Structural, electronic and magnetic properties of $Sn_{0.95}Ni_{0.05}O_2$ nanorods. Nanoscale. **3**(2), 642–653 (2011)
17. Sharma, M., Naji Aljawfi, R., Kumari, K., Chae, K.H., Dalela, S., Gautam, S., Alvi, P.A., Kumar, S.: Investigation of local geometrical structure, electronic state and magnetic properties of PLD grown Ni doped SnO_2 thin films. J. Electron. Spectrosc. Relat. Phenom. **232**, 21–28 (2019)
18. Verma, K.C., Kotnala, R.K.: Realizing ferromagnetic ordering in SnO_2 and ZnO nanostructures with Fe, Co, Ce ions. Phys. Chem. Chem. Phys. **18**(26), 17565–17574 (2016)
19. Aragón, F.H., Coaquira, J.A.H., Hidalgo, P., da Silva, S.W., Brito, S.L.M., Gouvêa, D., Morais, P.C.: Evidences of the evolution from solid solution to surface segregation in Ni-doped SnO_2 nanoparticles using Raman spectroscopy. J. Raman Spectrosc. **42**(5), 1081–1086 (2011)
20. Subramanyam, K., Sreelekha, N., Murali, G., Reddy, D.A., Vijayalakshmi, R.P.: Structural, optical and magnetic properties of Cr doped SnO_2 nanoparticles stabilized with polyethylene glycol. Physica B. **454**, 86–92 (2014)
21. Selvi, E.T., Sundar, S.M.: Popcorn like morphology and absence of room temperature ferromagnetism in Ni doped SnO_2 nanoparticles. J. Mater. Sci. Mater. Electron. **29**(1), 38–48 (2018)
22. Mazloom, J., Ghodsi, F.E., Golmojdeh, H.: Synthesis and characterization of vanadium doped SnO_2 diluted magnetic semiconductor nanoparticles with enhanced photocatalytic activities. J. Alloys Compd. **639**, 393–399 (2015)
23. Ahmed, A., Ali, T., Naseem Siddique, M., Ahmad, A., Tripathi, P.: Enhanced room temperature ferromagnetism in Ni doped SnO_2 nanoparticles: a comprehensive study. J. Appl. Phys. **122**(8), 083906 (2017)
24. Bouaine, A., Brihi, N., Schmerber, G., Ulhaq-Bouillet, C., Colis, S., Dinia, A.: Structural, optical, and magnetic properties of co-doped SnO_2 powders synthesized by the coprecipitation technique. J. Phys. Chem. C. **111**(7), 2924–2928 (2007)
25. Yang, H.M., Du, C.F., Jin, S.M., Tang, A.D., Li, G.S.: Enhanced photoluminescence property of SnO_2 nanoparticles contained in mesoporous silica synthesized with leached talc as Si source. Microporous Mesoporous Mater. **102**(1–3), 204–211 (2007)
26. Chetri, P., Saikia, B., Choudhury, A.: Structural and optical properties of cu doped SnO_2 nanoparticles: an experimental and density functional study. J. Appl. Phys. **113**(23), 233514 (2013)
27. Kar, A., Patra, A.: Optical and electrical properties of Eu^{3+}-doped SnO_2 Nanocrystals. J. Phys. Chem. C. **113**(11), 4375–4380 (2009)
28. Gu, F., Wang, S.F., Lü, M.K., Zhou, G.J., Xu, D., Yuan, D.R.: Photoluminescence properties of SnO_2 nanoparticles synthesized by sol-gel method. J. Phys. Chem. B. **108**(24), 8119–8123 (2004)
29. Kumari, M., Mondal, S., Madhuri, R., Sharma, P.K.: Synthesis of single phase $Fe_xSn_{1-x}O_2$ nanoparticles with enhanced structural,

optical and magnetic properties. J. Alloys Compd. **717**, 260–270 (2017)

30. Tan, Q.K., Kong, Z., Chen, X.J., Zhang, L., Hu, X.Q., Mu, M.X., Sun, H.C., Shao, X.C., Guan, X.G., Gao, M., Xu, B.H.: Synthesis of SnO_2/graphene composite anode materials for lithium-ion batteries. Appl. Surf. Sci. **485**, 314–322 (2019)
31. Choi, J.H., Park, S.-K., Kang, Y.C.: Superior lithium-ion storage performances of SnO_2 powders consisting of hollow nanoplates. J. Alloys Compd. **797**, 380–389 (2019)
32. Bhardwaj, N., Satpati, B., Mohapatra, S.: Plasmon-enhanced photoluminescence from SnO_2 nanostructures decorated with Au nanoparticles. Appl. Surf. Sci. **504**, 144381 (2020)
33. Ahmed, A., Siddique, M.N., Ali, T., Tripathi, P.: Defect assisted improved room temperature ferromagnetism in Ce doped SnO_2 nanoparticles. Appl. Surf. Sci. **483**, 463–471 (2019)
34. Chetri, P., Choudhury, B., Choudhury, A.: Room temperature ferromagnetism in SnO_2 nanoparticles: an experimental and density functional study. J. Mater. Chem. C. **2**(43), 9294–9302 (2014)
35. Parveen, N., Cho, M.H.: Self-assembled 3D flower-like nickel hydroxide nanostructures and their Supercapacitor applications. Sci. Rep. **6**, 27318 (2016)
36. Sharma, A., Varshney, M., Kumar, S., Verma, K.D., Kumar, R.: Magnetic properties of Fe and Ni doped SnO_2 nanoparticles. Nanomater. Nanotechnol. **1**(1), 29–33 (2011)
37. Jahnavi, V.S., Tripathy, S.K., Ramalingeswara Rao, A.V.N.: Structural, optical, magnetic and dielectric studies of SnO_2 nano particles in real time applications. Physica B. **565**, 61–72 (2019)
38. Maensiri, S., Pinitsoontorn, S., Phokha, S.: Structure and magnetic properties of Monodisperse Fe^{3+}-doped CeO_2 nanospheres. Nano-Micro Lett. **5**(4), 223–233 (2013)
39. Sonsupap, S., Ponhan, W., Wongsaprom, K.: Synthesis and room-temperature ferromagnetism in Co-doped In_2O_3 nanoparticles. J. Supercond. Nov. Magn. **29**(6), 1641–1646 (2016)
40. Pascariu, P., Airinei, A., Grigoras, M., Fifere, N., Sacarescu, L., Lupu, N., Stoleriu, L.: Structural, optical and magnetic properties of Ni doped SnO_2 nanoparticles. J. Alloys Compd. **668**, 65–72 (2016)
41. Coey, J.M.D., Venkatesan, M., Fitzgerald, C.B.: Donor impurity band exchange in dilute ferromagnetic oxides. Nat. Mater. **4**(2), 173–179 (2005)
42. Coey, J.M.D., Douvalis, A.P., Fitzgerald, C.B., Venkatesan, M.: Ferromagnetism in Fe-doped SnO_2 thin films. Appl. Phys. Lett. **84**(8), 1332–1334 (2004)
43. Wang, H.X., Yan, Y., Du, X.B., Liu, X.Q., Li, K., Jin, H.M.: Origin of ferromagnetism in Ni-doped SnO_2: first-principles calculation. J. Appl. Phys. **107**(10), 103923 (2010)
44. Aragon, F.H., Coaquira, J.A., Hidalgo, P., Brito, S.L., Gouvea, D., Castro, R.H.: Structural and magnetic properties of pure and nickel doped SnO_2 nanoparticles. J. Phys. Condens. Matter. **22**(49), 496003 (2010)
45. Manikandan, D., Boukhvalov, D.W., Amirthapandian, S., Zhidkov, I.S., Kukharenko, A.I., Cholakh, S.O., Kurmaev, E.Z., Murugan, R.: An insight into the origin of room-temperature ferromagnetism in SnO_2 and Mn-doped SnO_2 quantum dots: an experimental and DFT approach. Phys. Chem. Chem. Phys. **20**(9), 6500–6514 (2018)